



Fabrication of stable NiO/Fe₂O₃ heterostructure: A versatile hybrid material for electrochemical sensing of glucose, methanol and enhanced photodecomposition and/photoreduction of water contaminants



Sumanta Jana^a, Anup Mondal^b, Ashutosh Ghosh^{a,*}

^a Department of Chemistry, University College of Science, University of Calcutta, 92, A. P. C. Road, Kolkata 700009, India

^b Department of Chemistry, Indian Institute of Engineering Science and Technology, Shibpur 711103, India

ARTICLE INFO

Keywords:

Thin film heterostructure
Sensor
Photodecomposition
Photo reduction

ABSTRACT

The p-NiO/n- α -Fe₂O₃ heterostructures have been synthesized following three sequential steps. First, electrochemically NiO thin films are synthesized on FTO substrate, Fe₂S thin films are then electrodeposited onto NiO surface (FTO/NiO/Fe₂S). On air annealing FTO/NiO/Fe₂S at 600 °C results NiO/Fe₂O₃, a completely different heterostructure. Electrochemical study shows that the sensor (NiO/Fe₂O₃) has sensitivity 1437 μ A mM⁻¹ with detection limit 1.03 μ M for glucose. The electrode is successfully applied to assay glucose concentration in human blood. The same electrode also exhibits prominent electrocatalytic activity to oxidise methanol in alkaline medium. The coupled semiconductor (NiO/Fe₂O₃) shows enhanced efficiency towards the photodecomposition of phenol and commercial dyes e.g., Congo red (CR), Rhodamine B (RhB). Again photo reduction ability of Cr(VI) is confirmed by the heterostructure which registers a remarkable reduction of toxic Cr(VI) to non toxic Cr(III). The present material can be used as a single platform to clean up the various environmental issues.

1. Introduction

Semiconductor nano heterostructures are given more attention for its enhanced electrochemical and photocatalytic performances which have brought significant progress to applied fields [1,2]. Nickel oxide (NiO) is one of such technologically important and chemically stable p-type electrochromic material, widely used as electrochemical supercapacitors [3], electrodes [4] gas sensors [5] etc. Due to low conductivity of NiO, it could not be applied effectively in various applications. It shows low degradation efficiencies towards the removal of waste water contaminants [6]. It is not suitable as electrode material to meet the basic requirement due to low specific capacity (theoretical) [7]. Hence, special attention should be given to enhance the conductivity of NiO modifying the structure through loading metal or metal oxide. This modification enhances surface area and electron transfer. Being a narrow band gap (~2.2 eV) material n-type Fe₂O₃ can be used extensively as electrodes for gas sensors and photocatalysts [8,9]. But low hole mobility, short lifetime of hole and high surface density of Fe₂O₃ restricted its applications [10]. Now coupling Fe₂O₃ with another semiconductor having suitable band gap energy can greatly enhance the catalytic activities of the composite material. It had been earlier demonstrated that the heterojunction nanostructures

formed by combining NiO and α -Fe₂O₃ showed remarkable enhancement in their applications [11,12]. Recent reports on synthesis of Fe₂O₃/NiO nanocomposites by framework-templated strategy [13], solvothermal [14], electrodeposition [15,16], CP (coordination polymer) annealing [17], electrospinning and calcination procedures [18] demonstrated use of Fe₂O₃/NiO as anode materials for lithium ion batteries, gas sensors, water oxidation, urea oxidation etc. But the present article imparts a signature in traditional synthetic strategies and versatility in applications for NiO/ α -Fe₂O₃ heterostructure. At present, conventional glucose sensors are available in market based on the electrochemical oxidation of glucose oxidase (GOD). It has high sensitivity but it suffers from high enzyme cost, complex matrix, tedious enzyme immobilization process, instability etc. Previous reports revealed that glucose sensors based on Ni metallic nanomaterials exhibits higher catalytic oxidation [19,20]. But the conductivity of NiO is not sufficiently high to show excellent electrochemical sensing. To enhance the conductivity of NiO, Shamsipur et al. synthesized MWCNT/NiO (multi-walled carbon nanotube) composite with enhanced glucose oxidation [21]. Lv et al. showed that graphene/NiO acts as an effective alternative hybrid material for enzyme-free glucose sensor [22]. We simply coupled NiO with Fe₂O₃ to enhance the activity of the new composite thin films. To our knowledge, this is the first report where

* Corresponding author.

E-mail addresses: Sumap143@gmail.com (S. Jana), agchem@caluniv.ac.in (A. Ghosh).

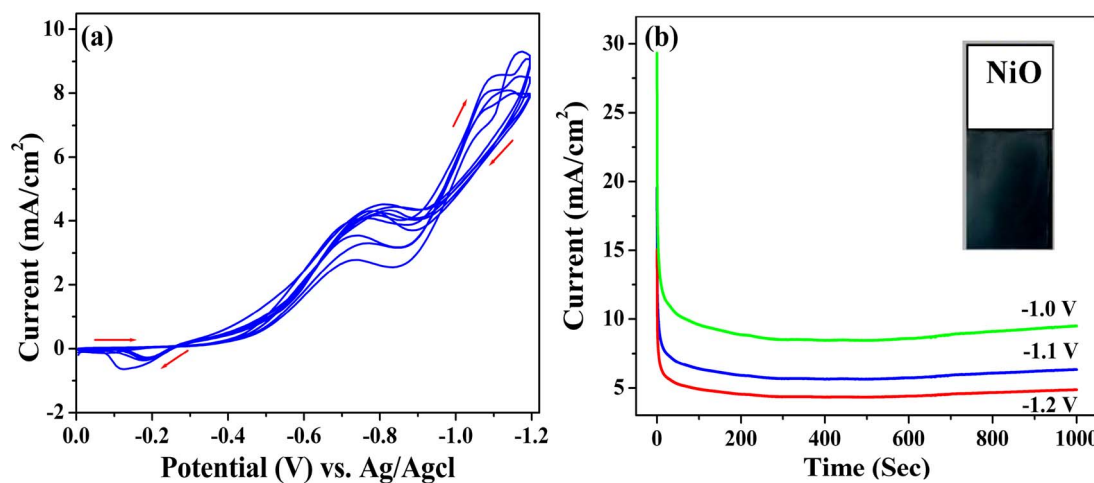


Fig. 1. (a) Cyclic voltammogram of working solution containing $\text{NiCl}_2 \cdot 6\text{H}_2\text{O}$, L(+) tartaric acid in KOH solution having pH 6.8 at a scan rate of 10 mV/S (b) Amperometric current density profile of NiO thin films at -1.0 V , -1.1 V and -1.2 V ; inset NiO thin film deposited at -1.1 V .

coupled NiO/Fe₂O₃ heterostructure has been successfully introduced as an effective electrode material for glucose estimation in human blood.

Further, methanol (CH₃OH) is a primary raw material and main precursor of CO, HCHO, and O₃. It is widely used in automobile industries. But high toxicity often affects blood and nervous systems of human beings. Hence, development of a convenient, reliable and non-toxic methanol sensor has become very imperative. Generally platinum based efficient and durable electro-catalyst is recommended for methanol sensing but it suffers from the poisonous affect of CO intermediates, slothful kinetics and high cost. Previously, several electro active materials based on Pt and Pt-binary electrodes were used for methanol oxidation [23,24]. On the contrary, alkaline DMFCs enable the use of non-noble, low-cost metal catalysts which show enhanced reaction kinetics and less corrosive environment [25,26]. Some promising non-Pt based electrocatalysts that were widely used in alkaline DMFCs are metallic nickel [27], nickel alloys [28,29] and nickel compounds [30,31]. Here we focused on direct electrochemical use of non-platinum based NiO/Fe₂O₃ electrode to oxidise methanol. This application triggers another scenario for the material development of fuel cells.

Photo decomposition has come out as an efficient environmentally caring technology for the decomposition of harmful dyes, phenols and toxic metals ions (Cr, Pb, Ni) [32,33]. To increase the efficiency of photocatalytic reactions, long lifetime and easy separation of photo-generated electron-hole pairs are two prime criteria that should be carefully addressed. Easy and effective separation of photogenerated electron-hole can be improved by coupling proper p-type and n-type semiconductor [34]. Light illumination on p-n heterojunction results a built-in electric field which drifts the photogenerated electron to conduction band of n-type material and holes to valence band of p-type material. This mechanism necessarily retards the rate of recombination between photogenerated electron and hole pairs [35]. In this article, photocatalytic study with synthesized NiO and NiO/Fe₂O₃ heterostructure were demonstrated with one anionic dye Congo red and one cationic dye Rhodamine B.

Photocatalytic activities of NiO and NiO/Fe₂O₃ thin films have also been described for phenol decomposition and Cr(VI) reduction which is a substitute of conventional powder photocatalysts. The powder photocatalysts have drawbacks relating to its recovery and agglomeration of particle during experimentation. However, using thin film as photocatalyst, we can easily overcome these drawbacks. Among the inorganic hazards and toxic contaminants in water, hexavalent chromium is identified as lethal mutagenic and carcinogenic to human being [36]. The elemental source of hexavalent chromium is Cr₂O₇²⁻ and CrO₄²⁻ which are mobile, water soluble and toxic to all living organisms

[37,38]. Because of high water solubility, it easily goes into living cells and forms reactive oxygen species (ROS) which causes serious oxidative injuries to cell constituents [39]. Presence of Cr(VI) above 0.05 mg/L (WHO standard) in drinking water causes lung, liver, kidney, and skin cancer [40]. In comparison to Cr(VI), the trivalent chromium (Cr(III)) is less harmful. Hence, reduction of Cr(VI) to Cr(III) has become an emerging research topic in environmental field. Previously, various techniques were employed to remove chromium e.g., cross flow microfiltration [41], reverse osmosis [42], ion exchange [43], photocatalytic reduction [44,45], adsorption [46] etc. However, in all these works, they did not receive advantages from photocatalytic reduction based on p-n heterojunction coupling for superior catalytic reduction of Cr(VI). In this article high degree of photo-decomposition/reduction of toxic substances by NiO/Fe₂O₃ photocatalyst are discussed for waste water treatment.

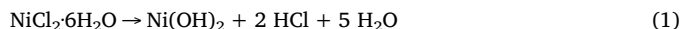
2. Experimental

Materials, instruments and some others are provided in Supporting information (SI).

2.1. Electrodeposition of NiO thin films

NiO thin films were electrodeposited on properly cleaned FTO glass substrate (thickness, 3.2 mm; resistivity, 8–10 Ω^2) at room temperature. In a chemical bath, 0.05 M nickel chloride ($\text{NiCl}_2 \cdot 6\text{H}_2\text{O}$) and 0.01 M L(+) tartaric acid were intimately mixed by constant stirring for 30 min. 50 mL 0.1 M KNO_3 solution was added into this reaction bath and stirred again for 20 min. The pH of the solution was 2.3 i.e. highly acidic. Now, dilute KOH solution was added dropwise to increase the pH to 6.8 and again stirred for an additional 10 min. Further addition of KOH leads to precipitation of Ni salt which is undesirable. The final volume was made up to 100 mL with distilled water. Electrodeposition was carried out in a three electrode system taking FTO as working electrode; a Pt foil and a saturated Ag-AgCl electrode were used as counter and reference electrodes respectively. Cyclic voltammetry (CV) showed an increment in current density (cathodic scan) beyond -0.3 V where reduction of Ni^{2+} ($\text{Ni}^{2+} \rightarrow \text{Ni}^{\circ}$) took place (Fig. 1(a)). After that an exponential increase in cathodic current density beyond -0.9 V indicates the growth of electrodeposited NiO followed by electrochemical reduction of $\text{Ni}(\text{OH})_2$ and water. Reverse anodic scan showed a relatively weak oxidation peak at -0.18 V due to the oxidation of electrodeposited metallic nickel (Ni°) species (deposited on FTO substrate during cathodic scan). The hydroxide anion generated in water reduction reacts with traces of nickel present onto FTO and ultimately

forms hydroxide Ni(OH)_2 . Therefore, it can be concluded that growth of NiO took place via hydroxide ion intermediate.



Chrono amperometry (CA) was performed to electrodeposit NiO thin films on FTO substrate. Three different potentials namely, -1.0 V , -1.1 V and -1.2 V were selected to electrodeposit NiO (Fig. 1(b)). Out of the three deposition potentials, it was observed that uniform, stable and well-adhered NiO films were obtained only at -1.1 V . Although current density at -1.0 V was maximum, but the deposited material was not well adhered to FTO substrate. Electrodeposition at -1.2 V results very fast and metallic Ni deposition which shows shiny gesture of metallic Ni on FTO substrate. The electrodeposited well adhered black films were washed thoroughly with running distilled water and methanol. Fig. 1(b) inset shows NiO thin film deposited at -1.1 V . The as synthesized thin films were air annealed at $400\text{ }^\circ\text{C}$ for 30 min for complete conversion to nickel oxide.

2.2. Electrodeposition of FeS_2 thin films on NiO

FeS_2 thin films were electrodeposited onto NiO thin films by slightly modifying our previously reported procedure [47]. Briefly, 10 mL 0.1 M Mohr salt ($\text{FeSO}_4(\text{NH}_4)_2\text{SO}_4 \cdot 6\text{H}_2\text{O}$) and 20 mL 0.1 M $\text{Na}_2\text{S}_2\text{O}_3$ were intimately mixed in a 100 mL chemical bath. The pH of the working solution was maintained to 3.8 by adding dilute H_2SO_4 . Now, in three electrode system as synthesized FTO/ NiO was taken as working electrode, standard Ag/AgCl and Pt foil were used as reference and counter electrodes respectively. Upper part of NiO electrode was covered with Teflon tape to avoid unwanted FeS_2 deposition on bare FTO. Amperometric technique was used to electrodeposit FeS_2 onto FTO modified NiO substrate where a constant potential -1.0 V was applied for 30 min. In this case, applied potential was increased to -1.0 V (previously it was -0.9 V for FTO substrate) because at -0.9 V we found very slow non-uniform deposition; it might be due to high resistance of NiO electrode. However, at -1.0 V a steady uniform deposition took place and a black layer of FeS_2 was formed onto entire NiO surface. As synthesized NiO/FeS_2 thin film was washed with running distilled water and dried at $200\text{ }^\circ\text{C}$ for 20 min in N_2 atmosphere.

2.3. Synthesis of $\text{NiO}/\text{Fe}_2\text{O}_3$ thin films

In this stage as synthesized NiO/FeS_2 thin films were air annealed at $600\text{ }^\circ\text{C}$ for an hour, black (colour) material transferred to red brown. The brown materials (thin films) so obtained were characterized with conventional techniques and processed for applications. A schematic diagram for the synthesis of $\text{NiO}/\text{Fe}_2\text{O}_3$ heterostructure was shown in Fig. 2.

3. Results and discussion

3.1. Structural and morphological characterization

Structural characterization of NiO thin films (as deposited and air annealed), NiO/FeS_2 and $\text{NiO}/\text{Fe}_2\text{O}_3$ thin films were carried out by X-ray diffraction (XRD) technique. Fig. 3(a)(i), (ii) represent the XRD pattern of as deposited, $400\text{ }^\circ\text{C}$ air annealed NiO thin films. As deposited NiO thin film shows low intense peaks and the diffraction peaks are not sharp which indicates amorphous nature of the material. Low crystalline NiO along with elemental Ni peak is evident from XRD image.

Fig. 3(a)(ii) represents XRD pattern of air annealed thin film. In this case, intensity of all the peaks are high and major diffractions are appeared from $(1\ 1\ 1)$, $(2\ 0\ 0)$, $(2\ 2\ 0)$, $(3\ 1\ 1)$ planes whose 2θ values and intensity counterpart well with the standard JCPDS data file # 47-1049 for cubic phase. The peak intensity of annealed NiO is higher than as

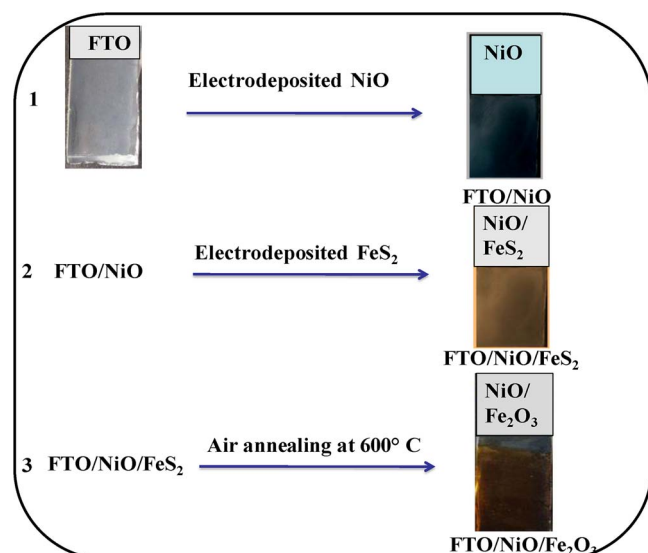


Fig. 2. Schematic diagrams of $\text{NiO}/\text{Fe}_2\text{O}_3$ thin film syntheses.

deposited NiO thin film which indicates that the air annealed material is more crystalline.

It exhibits maximum intense peak from $(2\ 0\ 0)$ plane along with other diffractions from $(1\ 1\ 1)$, $(2\ 2\ 0)$ planes. Fig. 3(b)(i) and (ii) are the XRD pattern of NiO/FeS_2 and air annealed NiO/FeS_2 thin film respectively. For NiO/FeS_2 thin film, major diffractions are observed from $(1\ 1\ 0)$, $(1\ 1\ 1)$ and $(2\ 2\ 1)$ planes of FeS_2 along with some NiO low intense peaks (● indicates NiO peak and * appears for FTO substrate). Comparing this diffraction with standard JCPDS card, it has been found that the peak positions and intensities are matches well with JCPDS # 74-1051 for orthorhombic FeS_2 . Fig. 3(b)(ii) shows XRD pattern of $600\text{ }^\circ\text{C}$ air annealed NiO/FeS_2 thin film where new major peaks are appeared from $(1\ 0\ 4)$, $(1\ 1\ 0)$ and $(1\ 1\ 3)$ planes. All the planes and their intensities match with standard JCPDS # 24-0072 for rhombo-centered phase for Fe_2O_3 . So, it can be concluded that, on air annealing the precursor NiO/FeS_2 thin film at $600\text{ }^\circ\text{C}$, a stable $\text{NiO}/\text{Fe}_2\text{O}_3$ heterostructure is generated.

As deposited SEM image of NiO shows compact morphology of almost spherical shaped NiO nanoparticles uniformly grown onto FTO substrate (Fig. 4(a)). Fig. 4(b) represents SEM image of annealed NiO thin film where a totally different morphology is generated. Due to air annealing a significant grain growth occurs among spherical NiO nanoparticles and results a porous flake like morphology. Fig. 4(c) is the SEM image of NiO/FeS_2 where agglomerated fused cluster type morphology is observed. Lower NiO layer is also visible in this SEM image. Now, air annealing this NiO/FeS_2 thin film at $600\text{ }^\circ\text{C}$ for an hour results a drastic morphological change. Low magnification SEM image (Fig. 4(d)) shows uniform spreading of interconnected porous nanoballs onto the entire FTO substrate. The material is extremely porous and consists of interconnected nanoballs. These nanoballs again comprise of indefinite numbers of two-dimensional nano petals which is clearly visible from high magnification SEM (Fig. 4(e)). These two-dimensional petals provide more inner space in nanoballs. Here, the nanoparticles are of much even sizes, and overall porous morphology will necessarily accelerate the inherent properties of the material. This unique morphology alerts further progressive study of $\text{NiO}/\text{Fe}_2\text{O}_3$ and is the key factor for its targeted applications. To detect the diameter of pores we tried for BET analysis but were unable to scrap off powder material from NiO and $\text{NiO}/\text{Fe}_2\text{O}_3$ thin films due to its strong adherence with FTO.

Fig. S1 represents the UV-vis absorption spectra of NiO , Fe_2O_3 and $\text{NiO}/\text{Fe}_2\text{O}_3$ thin films. The absorption spectrum of NiO (Fig. S1(a)) showed a sharp absorption from $\sim 00\text{ nm}$. From this absorption,

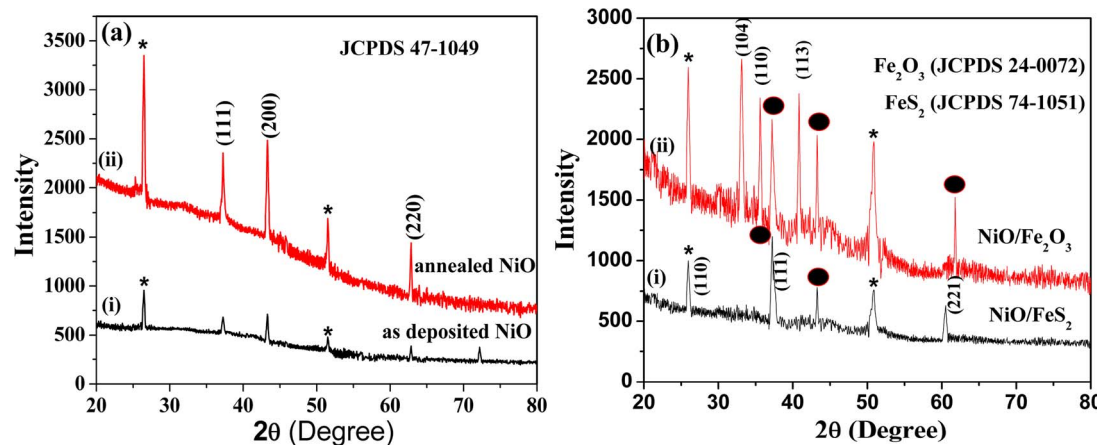


Fig. 3. XRD patterns of (a) as deposited and annealed NiO thin films (b) NiO/FeS₂ thin film and NiO/Fe₂O₃ thin film.

corresponding band gap was calculated using Tauc's relation $[(ah\nu)^n = A(\hbar\nu - E_g)]$ and found to be 3.5 eV (where, $\hbar\nu$ is incident photon energy, 'A' is a constant and the exponent 'n' is determined by the type of electronic transition causing the absorption). Fig. S1(b) represents the UV–vis spectrum of Fe₂O₃ thin film where a sharp rise in absorbance was observed from 550 nm. Optical band gap was calculated from the absorption value and found to be 2.4 eV (Fig. S1(b) inset). Fig. S1(c) represents UV–vis absorption spectrum of NiO/Fe₂O₃ thin film. The plot $(ah\nu)^2$ versus $\hbar\nu$ was drawn and found that the plot is semi parabolic nature. It has two prominent inflexions which indicate two transitions occurring in annealed NiO/Fe₂O₃ thin film. The band gap energy (E_g) calculation revealed that these phases exist at 2.7 and 3.1 eV, corresponds to Fe₂O₃ and NiO.

To clarify the composition and chemical state of elements in NiO and NiO/Fe₂O₃ thin films XPS measurements were carried out. Fig. S2(a) is the wide range spectrum of NiO thin film (survey spectra), presence of Ni 2p, Sn 3d and O 1s peaks confirms it. Fig. S2(b) and (c) are the XPS spectra for the Ni 2p and O 1s. XPS spectrum of Ni 2p (Fig. S2(b)) shows two main peaks separated at binding energies 855.7 eV and 872.3 eV for Ni 2p_{3/2} and Ni 2p_{1/2} respectively, clearly suggests presence of NiO. O 1s spectrum has two closely separated peaks (Fig. S2(c)) correspond to the binding states of Ni²⁺ (529.6 eV) and Ni³⁺ (532.0 eV) respectively [48]. So, the presence of Ni²⁺ and Ni³⁺ ions in NiO thin film confirm that the material is nonstoichiometric. Nonstoichiometric NiO has Ni²⁺ vacancies, therefore to maintain electrical neutrality some Ni²⁺ may oxidize to Ni³⁺. So it can be concluded that our synthesized material (NiO) is nonstoichiometric and presence of Ni₂O₃ confirms it. Fig. 5 displays full scanned XPS spectra of NiO/Fe₂O₃ nanostructure; it confirms the existence of Fe, Ni, and O elements into the heterostructure. Fig. 5(a) is the wide range survey spectrum of NiO/Fe₂O₃ thin film which confirms the presence of Ni 2p, Fe 2p, and O 1s. XPS spectrum of Ni 2p (Fig. 5(b)) comprises of four easily distinguishable peaks (two main peaks and two satellite peaks). For Ni 2p_{3/2} main peak and satellite peak appear at 856 eV and 861 eV respectively. Whereas for Ni 2p_{1/2} main peak and its satellite peak appear at 872.5 and 880 eV respectively, it again confirms presence of NiO in the heterostructure. Fig. 5(c) represents XPS spectrum of Fe 2p where two closely separated doublet peaks are appeared at 713 eV and 724 eV for Fe 2p_{3/2} and Fe 2p_{1/2} of Fe₂O₃. XPS spectrum of O 1s shows (Fig. 5(d)) one most intense peak at 531.6 eV due to O bonded regular oxide crystal (Ni³⁺) and one weaker peak located at 529 eV is assigned to the binding states of Ni²⁺.

Two-probe I–V measurements of NiO and NiO/Fe₂O₃ were performed to know the type of deposited material (n type or p type) and to prove formation of heterostructure in NiO/Fe₂O₃. Two contact points were made where bottom contact was taken from FTO substrate (an n-type semiconductor) and top contact was taken from the upper surface of deposited layer. Au/Pd alloy was used as contact material. Fig. S3(a)

shows the two-probe I–V plot of NiO thin films. It shows characteristic diode formation between FTO and NiO i.e. formation of p–n junction. So it is clear that the deposited NiO on FTO substrate is no doubtly a p type semiconductor. I–V nature also informs that the threshold voltage for NiO is high and the Zener breakdown occurs at a reverse bias at around –1.2 V. Fig. S3(b) represents I–V plot of NiO/Fe₂O₃ thin films; it shows better diode characteristics than NiO. Here, threshold voltage is increased more sharply and Zener breakdown occurs at further reverse bias at around –1.75 V. The heterojunction indicates a good sign for non ohmic diode material. So, it can be concluded that the NiO/Fe₂O₃ is a layer by layer thin film material (heterostructure) and enhancement of diode characteristics is due to Fe₂O₃ incorporation.

Electrochemical study was carried out in a chemical bath taking 1 M NaOH as electrolyte. Synthesized thin films were used as working electrode, Ag/AgCl as reference and platinum as counter electrode. Fig. S4 shows Mott–Schottky plots obtained from $1/C^2$ versus applied potential for Fe₂O₃ and NiO/Fe₂O₃ thin films at constant frequency of 10 kHz. For Fe₂O₃ a positive slope was observed indicating the existence of electrons as the majority carriers i.e., n type semiconductor (Fig. S4(a)). On the otherhand, NiO/Fe₂O₃ heterostructure shows both positive and negative slopes corresponding to the n and p type conductivity (Fig. S4(b)). Hence, it indicates formation of p–n-heterojunction [49]. The intercept of linear plots gives flat band potential which is –0.5 V for Fe₂O₃ and –0.32 V for NiO/Fe₂O₃ thin films (vs. Ag/AgCl).

3.2. Glucose sensing

Glucose was taken as a model compound because it was given more attention in diagnosis and used extensively in food processing from several past years. The sensing experiment was carried out in a three-electrode system, where as synthesized NiO/Fe₂O₃ thin film was taken as working electrode and a Pt wire, saturated Ag–AgCl electrode were employed as counter and reference electrodes, respectively. Fig. 6(a) shows cyclic voltammogram of NiO/Fe₂O₃ with gradual addition of glucose in 0.1 M NaOH solution. From the figure it is clear that with increasing glucose concentrations, current height in anodic sweep increases successively; indicates that the electrode has efficiency to oxidise glucose. Here, oxidation potential of glucose is ~0.46 V. To calculate apparent Michaelis–Menten constant K_M^{app} and the maximum current for NiO/Fe₂O₃ electrode conventional Michaelis–Menten equation is used.

$$I_{ss} = (I_{max} \times [S]) / K_M^{app} + [S] \quad (3)$$

Where I_{ss} is steady-state current, I_{max} is current maximum, $[S]$ is substrate concentration.

Fig. 6(b) shows typical steady state amperometric responses of NiO/Fe₂O₃ and NiO electrodes with gradual addition of glucose at constant

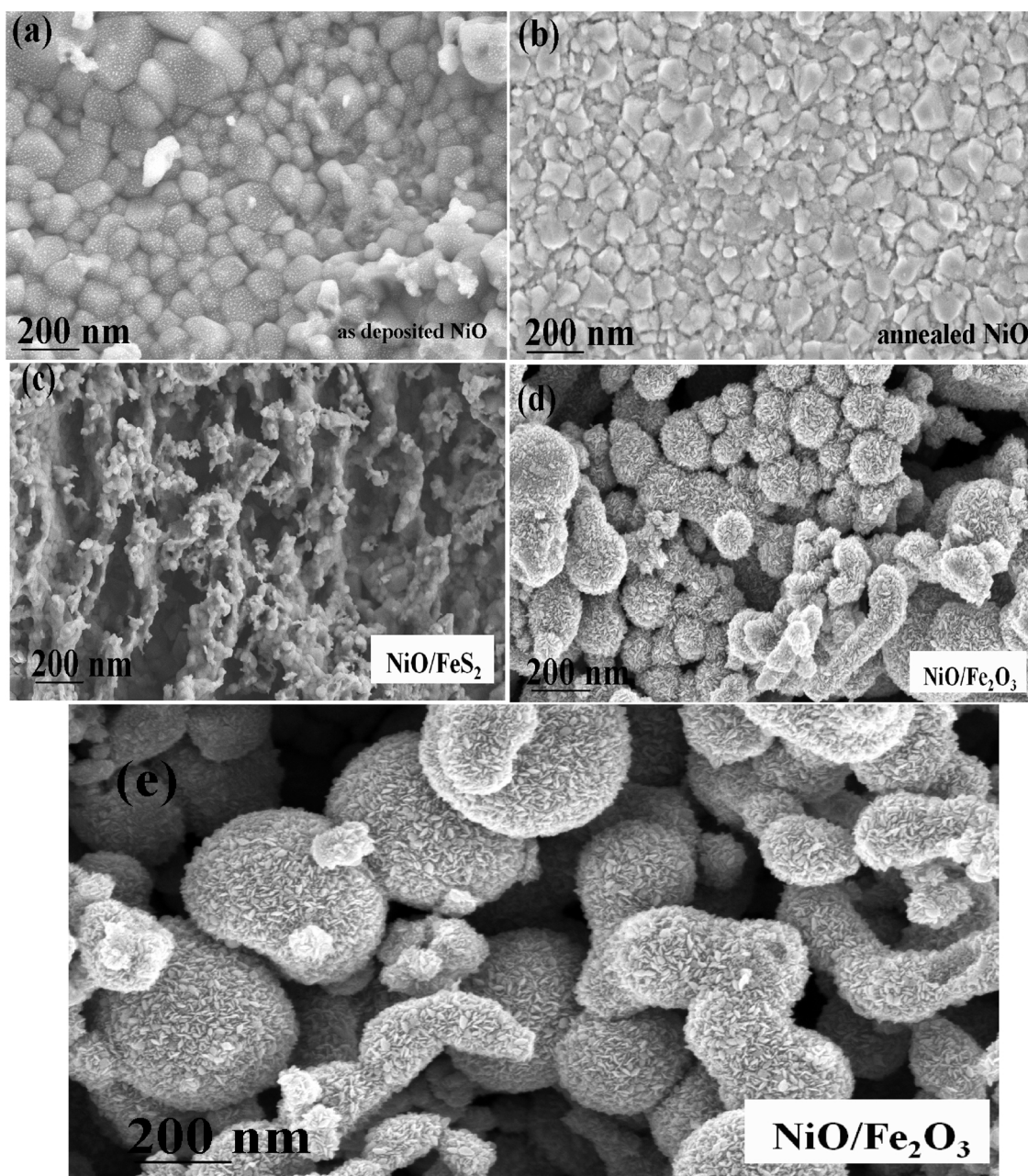


Fig. 4. FESEM images of (a) as deposited and (b) 400 °C air annealed NiO thin film (c) NiO/FeS₂ and (d) NiO/Fe₂O₃ thin film at low magnification (e) NiO/Fe₂O₃ thin film at high magnification.

potential (0.46 V). When an aliquot amount of glucose (μ M range) was added to the working solution (pH 9) a step wise increment in current density was observed in kinetics plot. We had tried the same analysis with the neutral buffer solution, but no increment in current density was detected which indicates the crucial role of OH[−] in the alkali media. The response time of the sensor was found to be ~8 s and the attainment of steady state current was an additional 4 s. The result indicates very fast electrocatalytic response of the modified NiO electrode. From the calibration curves (Fig. S5(a)) a linear relationship was obtained in the concentration range of 1–450 μ M with correlation coefficient 0.978 for NiO/Fe₂O₃. The sensitivity of this modified sensor was calculated to 1437 μ A mM^{−1} (correlation coefficient 0.9996) with detection limit 1.03 μ M. The calibration curve shows a linear increase in current with successive addition of glucose and after a certain period current reaches to a steady value which illustrates Michaelis–Menten type behavior.

Using Lineweaver–Burk model, the apparent Michaelis–Menten constant ($K_{app}M$) was calculated and found to be 4.08 mM, 25.6 mM for NiO/Fe₂O₃ and NiO electrodes respectively (Fig. S5(b)). The smaller $K_{app}M$ value for NiO/Fe₂O₃ indicates higher affinity towards glucose oxidation. A comparison of different glucose sensors was enlisted in Table S1 (Supporting information) [50–57] from the table it can be concluded that our synthesized NiO/Fe₂O₃ is fairly suitable as an active electrode for glucose detection.

3.2.1. Anti-interference activity study

It is well-known that chloride ion can poison electrodes. Therefore, anti poison study should be carried out in order to judge its applicability in real blood sample. In this study various amounts of chloride ions in the range of 20–400 mM were added into the standard solutions of glucose (mM concentration) for 5 min to evaluate the interference. The result indicates that the chloride ion does not interfere in

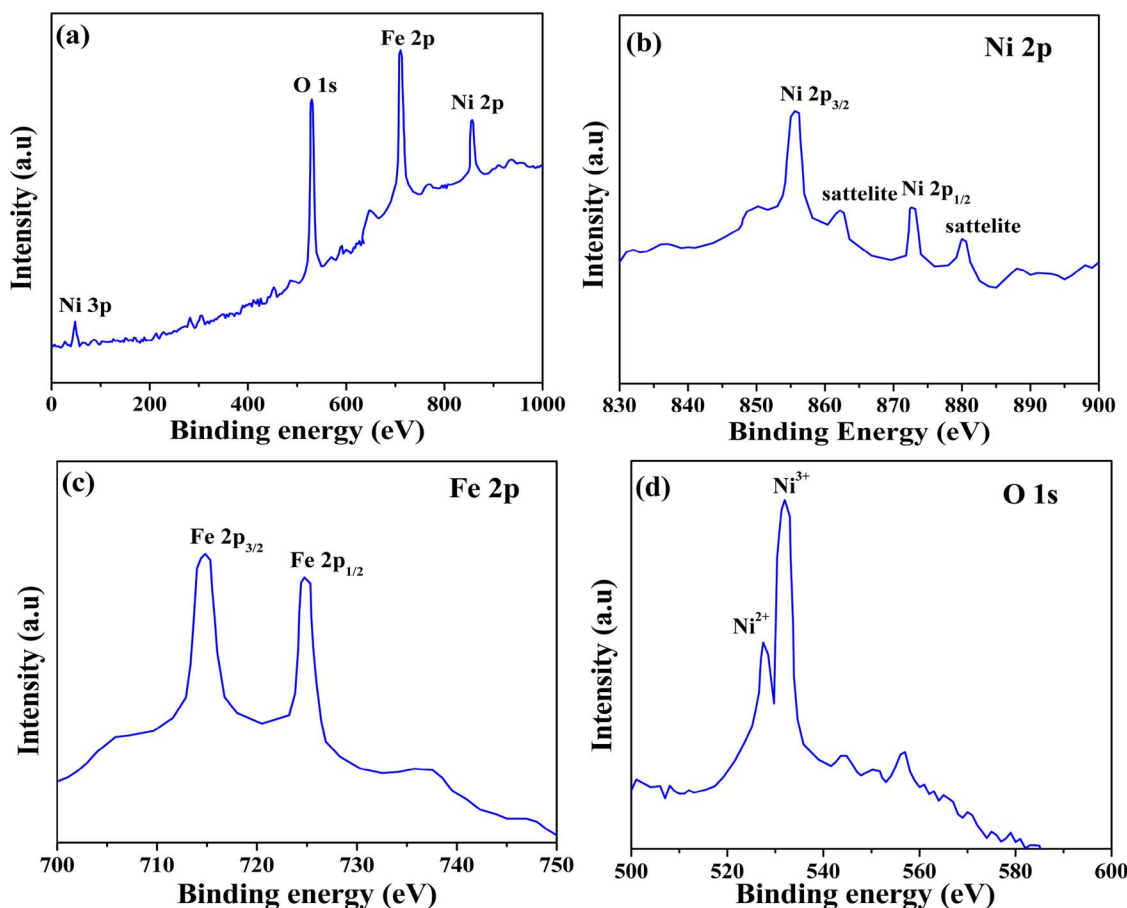


Fig. 5. XPS spectra of $\text{NiO}/\text{Fe}_2\text{O}_3$ thin film (a) survey spectrum (b) Ni 2p spectrum (c) Fe 2p spectrum (d) $\text{O}1\text{s}$ spectrum.

measurement even when its concentration is as high as 400 mM. So, we can certify that the electrode is quite suitable for measuring human blood serum samples containing chloride ions up to 400 mM. Selectivity and anti-interference ability of the biosensor was again investigated by addition of specific amounts of electroactive species. A major challenge in non-enzymatic glucose sensing is the inherent interferences where uric acid (UA), ascorbic acid (AA) and dopamine (DA) are unavoidable in practical sense. The standard physiological ratio of glucose:interferent is more than 30:1. Here, we have added the interferents ten times extra, so the ratio comes to 3:1. With this high concentration of interferents, we want to judge sensitivity of $\text{NiO}/\text{Fe}_2\text{O}_3$ in presence of concentrated interferents during glucose sensing. Fig. S6 depicts the

sensitivity of the present sensor in glucose sensing by adding 10 μM AA, 10 μM UA and 10 μM DA interferents at 0.46 V at pH 9. The result shows that such high concentrations of AA, UA and DA have no significant influence on glucose sensing. To examine the relative sensitivity of the proposed sensor towards glucose sensing amperometric experiments were carried out using maltose, lactose and fructose in place of glucose in same working solution at 0.46 V (Fig. S7). The corresponding relative sensitivity of the samples is shown in Fig. S8. These observations obviously indicate that our $\text{NiO}/\text{Fe}_2\text{O}_3$ heterostructure has high affinity to sense glucose exclusively.

Estimation of glucose concentration in real blood samples was carried out by collecting the blood samples from voluntary individuals.

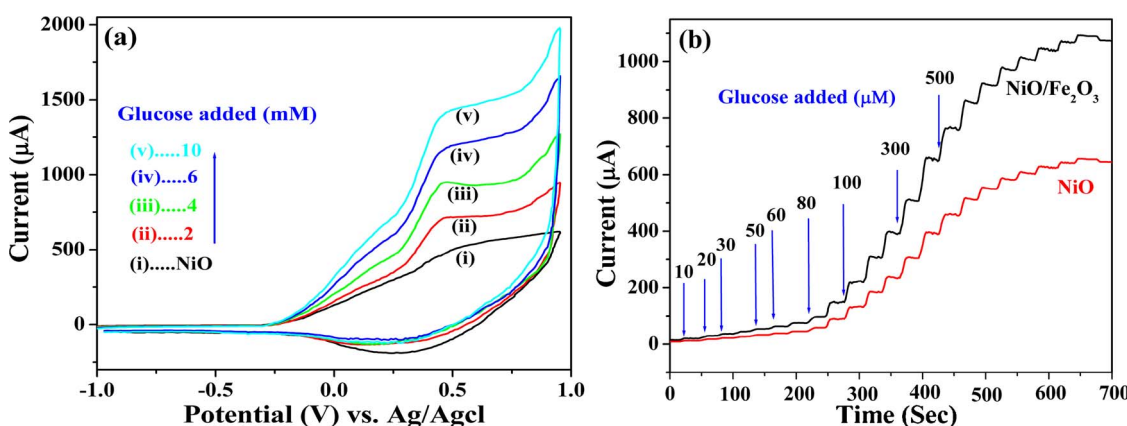


Fig. 6. (a) Cyclic voltammograms of $\text{NiO}/\text{Fe}_2\text{O}_3$ and NiO electrodes in 0.1 M NaOH (pH 9) with successive addition of glucose (2–10 mM) at scan rate 50 mV/s (vs. Ag/AgCl) (b) Amperometric responses of $\text{NiO}/\text{Fe}_2\text{O}_3$ and NiO with successive addition of glucose (μM range) in same working solution at an applied potential of 0.46 V.

Table 1

Comparative study of glucose concentration in human blood serum samples.

Sample No.	Glucose concentration (mM) measured by the local pathology	Glucose concentration (mM) Measured by the present NiO/Fe ₂ O ₃ electrode	Relative Error (%)
1	7.35	7.52	2.3
2	7.19	7.28	1.2
3	5.20	5.32	2.3

Experiment was performed in compliance with all institutional and national guidelines as per the Indian Council of Medical Research (ICMR 2006): Biomedical Research on Human Participants; the experiment was approved by Institutional Ethics Committee (EC/HBG3407/1). To find its potential use in real sample analysis, NiO/Fe₂O₃ was used as working electrode to measure the concentration of glucose in human blood samples. First serum samples were extremely diluted. From each sample 100 μL was taken out and administered into 10.0 mL 0.1 M NaOH solution bath. The current response was recorded at 0.46 V. Table 1 represents the outcomes of the proposed sensor for three different serum samples. It was found that experimental results are quite comparable with the results obtained from a registered pathology centre. It indicates that the NiO/Fe₂O₃ is promising one for practical application of glucose estimation.

3.2.2. pH and temperature (T) dependent activity for glucose sensing

The stability and the performances of the proposed sensor were analysed over a wide range of pH (2–11) and temperature (10–80 °C). It was found that maximum electrocatalytic performance occurred at pH 9 (Fig. S9(a)). Temperature variation study revealed that the maximum catalytic activity was found at 40 °C (Fig. S9(b)).

3.3. Methanol oxidation

Here, electrodeposited NiO/Fe₂O₃ on FTO substrate was directly used as a non-Pt based working electrode to study methanol oxidation without adding any binder or conducting agent. All the electrodes (same electrode arrangement was followed as it was in glucose sensing) were dipped into 50 mL of 0.5 M NaOH chemical bath and degassed by purging pure N₂ for 10 min. Fig. 7(a) represents cyclic voltammogram of NiO thin film with gradual addition of 0.01, 0.02, 0.03, 0.04, 0.05, and 0.06 M methanol in alkaline solution. In CV scan anodic current increases sharply from 0.2 V onwards due to transition of Ni (II) to Ni (III) and highest current density was observed at 0.5 V.

Fig. 7(b) represents the cyclic voltammogram of NiO/Fe₂O₃ thin film with gradual addition of 0.01, 0.02, 0.03, 0.04, 0.05, and 0.06 M methanol in same working solution. In this case, the current density increased to ~10 times more than NiO electrode and highest current density was observed at 0.47 V which is lower than NiO electrode (0.5 V). It indicates that NiO/Fe₂O₃ has higher affinity to oxidise methanol than NiO.

The stability of an electrode is a vital factor in its overall performances and the chronoamperometric technique is the best way to judge the stability of any electrode. Fig. 7(c) shows current-time curves of NiO and NiO/Fe₂O₃ electrodes in same working solution (without methanol). The high current density of NiO/Fe₂O₃ electrode necessarily indicates better stability and activity of the heterostructure compared to NiO.

3.3.1. Stability performance of the electrode

Stability or reusability is a prime criterion for any good electrode. After both experiments the electrodes were washed properly with running distilled water and dried in N₂ atmosphere. Then they were kept in a sealed glass tube. When NiO/Fe₂O₃ electrode was kept at 4 °C in a sealed tube for 20 days and used again for the same experiments

(glucose and methanol sensing) about 90% activity was noted.

3.4. Photodecomposition of phenol

According to WHO's recommendation phenol is a major pollutant of surface and inland water and the exposure limit of phenol in inland water should not be higher than 0.02 mg/L [58]. But the secure level decomposition within this limit is really very difficult due to its high stability and water solubility. Four NiO or and NiO/Fe₂O₃ thin films each having surface area 2 × 1 cm² were vertically placed into (5 × 10⁻⁴ mol/L) aqueous solution of phenol. A 200 W tungsten lamp (≥410 nm) was taken as a light source and was placed 10 cm apart from dye solution. 1 M NaNO₂ solution was used as UV cut off filter. At an interval of ten minutes 5 mL phenol solution was withdrawn and the changes in concentration were monitored by PL spectrophotometer, at an excitation of 280 nm. Fig. S10(a) shows fluorescence emission spectra of phenol in presence of NiO thin films where maximum emission peak was observed at ~310 nm. This is the characteristic fluorescence emission of phenol. The fluorescence intensity decreases gradually with increasing exposure time under light irradiation. This decrease in peak intensity with time indicates decomposition of phenol. Fig. S10(b) shows relative conc. vs time plot to calculate % of decomposition. From the kinetics plot ~57% decomposition was calculated for NiO thin films within 100 min. In case of coupled semiconductor (NiO/Fe₂O₃) an enhanced photodecomposition was observed and intensity of residual phenol decreases more rapidly with increasing exposure time (Fig. 8(a)). Fig. 8(b) shows relative conc. vs time plot where intensity decreases to ~80% within 100 min. Compared to the former experiment (where NiO thin films were used) an enhanced decomposition of 23% was observed for NiO/Fe₂O₃ heterostructure within same time frame.

3.5. Photodegradation of dye

In phenol decomposition we have seen that NiO/Fe₂O₃ heterostructure is more efficient to decompose phenol than NiO. Will this coupled heterostructure able to decompose toxic dyes with same efficiency? To find out the answer we proceeded for dye degradation where one anionic dye (CR: C₃₂H₂₂N₆Na₂O₈S₂) and one cationic dye (Rhodamine B: C₂₈H₃₁C₁N₂O₃) were taken as model dye. In this case also four thin films of active surface area 2 × 1 cm² were vertically immersed into a 50 ml (5 × 10⁻³ M) aqueous solution of congo-red (CR) and/or rhodamine B (RhB). Same light source and cut off filter were used to perform the experiment. At specific time intervals (10 min), 5 mL of dye solution was withdrawn from the stock, centrifuged and the changes in concentration were monitored by UV-vis spectroscopy. In case of CR maximum absorption occurs at ~490 nm (Fig. 9(a)) and absorption intensity decreases gradually with exposure time. Fig. 9(b) represents the kinetics of CR degradation. It shows almost no degradation for NiO and NiO/Fe₂O₃ in absence of light. But in presence of light NiO shows only ~40% degradation whereas for NiO/Fe₂O₃ heterostructure percentage of degradation is increased to ~96% within 100 min (efficiency increases more than two times).

Fig. 10(a) shows the absorption spectra of RhB in the presence of NiO/Fe₂O₃ thin films. Here maximum absorption occurs at ~550 nm which is the λ_{max} of RhB. The gradual decrease in intensity with irradiation time confirms RhB degradation. Kinetics plot (Fig. 10(b)) shows only 29% degradation of RhB by NiO thin films in presence of light. On the contrary, for the coupled semiconductor this efficiency is increased to 85% (efficiency increases about three times). So, the prepared NiO/Fe₂O₃ heterostructure is more efficient to remove anionic dye than cationic dye in neutral solution.

It is well established that photodecomposition reactions proceed mainly by the active participation of reactive oxygen species O₂[−], OH^{*} and H₂O₂ [59]. The essential requirement for any photodecomposition or degradation is generation of maximum number of separated photo-

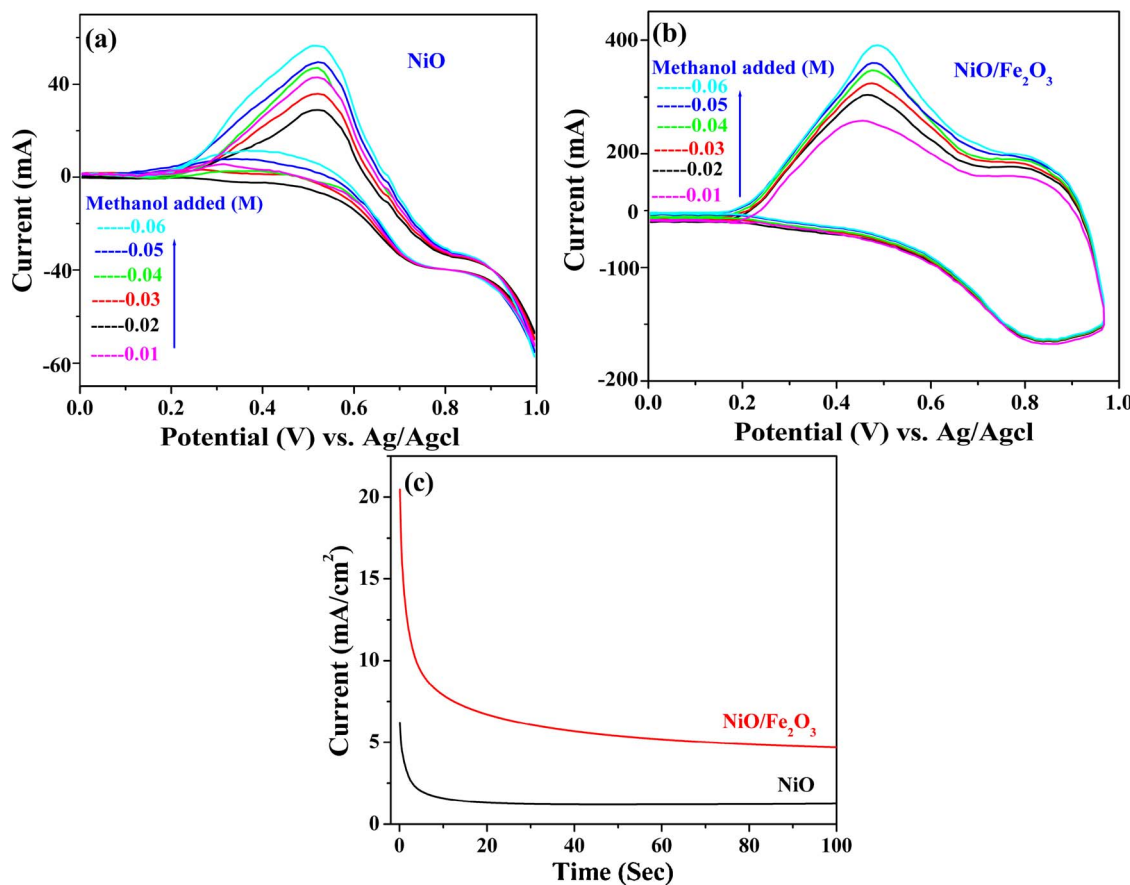


Fig. 7. Cyclic voltammograms of (a) NiO and (b) NiO/Fe₂O₃ thin film in 0.5 M NaOH with gradual addition of methanol at 50 mV/s scan rate (c) Current-time curves of NiO and NiO/Fe₂O₃ thin films.

excited electrons (e^-) and holes (h^+) from a photocatalyst by the absorption of light. The electron reacts with oxygen (O_2) and generates super oxide anion (O_2^-). The O_2^- anion further readily reacts with H_2O and generates OH^* (hydroxyl) radicals which is one of the major active species for decomposition. Similarly hole reacts with H_2O and forms activated OH^* (hydroxyl) radicals. Again superoxide radical (O_2^-) reacts and generate hydrogen peroxide (H_2O_2). Similarly, reaction between active hydroxyl radicals results reactive peroxide. These O_2^- , OH^* and H_2O_2 are the major reactive oxidative species for the decomposition of organic pollutants. The efficiency (to degrade/decompose dyes or toxic materials) of a particular photocatalyst will be higher if it generates reactive species at higher rate with lesser time

[60].

These reactive species can be generated smoothly when the material inhibits electron hole recombination and in this case oxygen plays an important role. Oxygen prevents recombination/assimilation of electron-hole in dye solution by trapping electrons and acts as an oxidant for hydroxyl adducts [61]. It leads to better interfacial charge transfer to the adsorbed substrate. Decomposition of dyes correspond to hydroxylation by active hydroxyl radicals (OH^*) where excited coupled NiO/Fe₂O₃ heterostructure gets sufficient activation energy and reacts with OH^* radicals and produce CO_2 and H_2O as final product [62,63]. In case of phenol decomposition the common intermediates viz., catechol, hydroxyhydroquinone, hydroquinone, benzoquinone etc. are

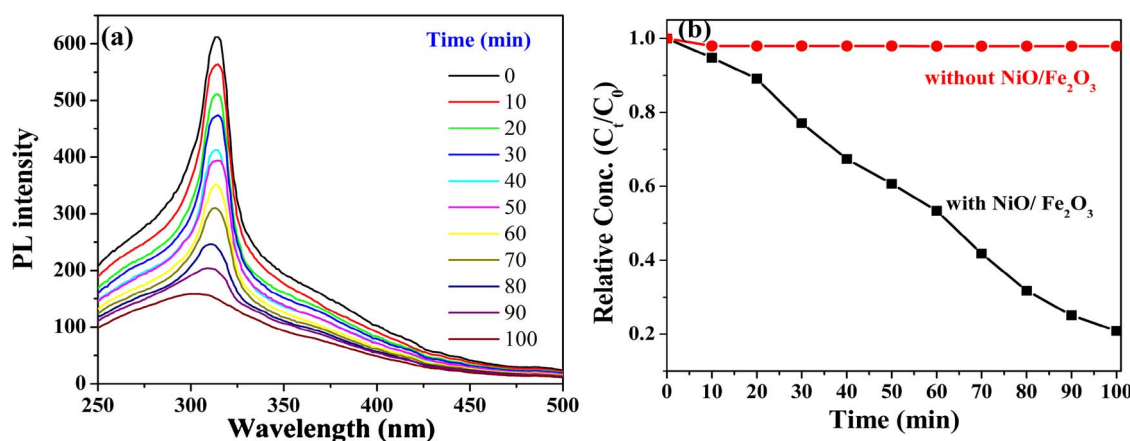


Fig. 8. (a) Spectral change of phenol solution with time and light irradiation in presence of NiO/Fe₂O₃ thin films (b) Intensity of residual phenol as a function of irradiation time in presence of NiO/Fe₂O₃ thin films.

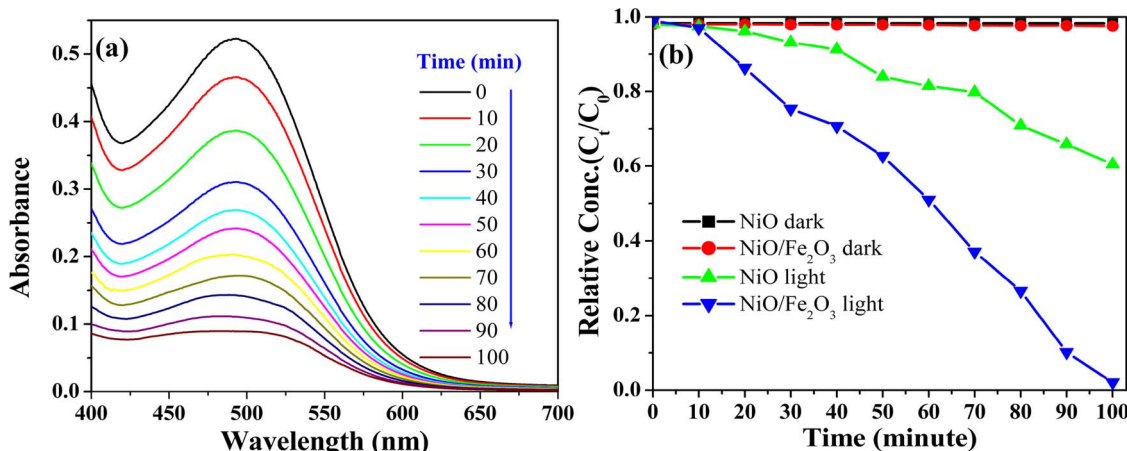


Fig. 9. (a) Spectral change of CR dye solution in the presence of light and NiO/Fe₂O₃ thin films. (b) Reaction profile of CR degradation against specific time intervals under various conditions.

also expected to form during the decomposition [64]. In photocatalysis electron-hole recombination is a major drawback for most of the semiconducting materials. In case of Fe₂O₃, the energy difference between conduction band and valence band is only 2.2 eV, where the chances of recombination are high. However, when Fe₂O₃, is placed on the surface of NiO a strong interaction is established followed by band bending between them (Fe₂O₃ and NiO). This leads to very slow recombination of excited photoelectrons with holes. More slowly the electron-hole recombination faster is the catalytic activity. The enhanced reactivity of the heterostructure can be explained by band diagram. Under light irradiation, the photogenerated electrons on the conduction band (CB) of Fe₂O₃ are transferred to the CB of NiO to decrease potential energy and holes on valence band (VB) of NiO migrate to the VB of Fe₂O₃ simultaneously. This cyclic easy transport of electron-hole within NiO/Fe₂O₃ matrix enables the separation of photogenerated electrons and holes. Schematic representation of band diagram for NiO/Fe₂O₃ was shown in Fig. S11.

3.6. Photo reduction of Cr (VI)

Here exact same set of arrangement was used (arrangement for phenol decomposition /dye degradation) for photo reduction of dichromate solution (5×10^{-4} mol/L) with the synthesized thin films. Fig. 11 shows the photocatalytic reduction spectra of aqueous Cr(VI) at pH 2 under visible light irradiation in presence of as-synthesized NiO/Fe₂O₃ thin films. The absorption spectra of Cr(VI) centered at 350 nm

decreases with the exposure time (Fig. 11(a)). It has been observed that the synthesized NiO/Fe₂O₃ thin films show remarkable photo reduction ability ~100% to reduce Cr₂O₇²⁻ within 90 min of visible light irradiation Fig. 11(b). Test was carried out in presence of NiO/Fe₂O₃ but in absence of light irradiation where no change of Cr(VI) absorption was found (Fig. S12(a)). Experiment was also performed under visible light irradiation but in absence of catalyst (Fig. S12(b)) and no change in absorption of Cr(VI) was observed even after several hours. It directs that only photolysis is not able to drive the reduction of Cr(VI). Hence, it can be concluded that the removal of aqueous Cr(VI) is no doubtly a photocatalyst-driven reduction of Cr(VI), rather than a simple physical adsorption of Cr(VI).

Photocatalytic reduction of Cr(VI) to Cr(III) is mainly promoted by photoexcited electrons, and here also, better electron–hole separation is the prime criterion. It can be well explained by the schematic diagram as stated in Fig. S11. Fe₂O₃ is a low band gap semiconductor ($E_g = 2.2$ eV), where the chances of recombination between electron and hole are quite high. However, when Fe₂O₃, is coupled with higher band gap NiO; a strong interaction leads to efficient band bending between Fe₂O₃ and NiO. It slows down recombination of excited photoelectrons with holes. Under light irradiation, photogenerated electrons on the conduction band (CB) of Fe₂O₃ are transferred to the CB of NiO to decrease potential energy. Now CB electrons of NiO readily react with O₂ and forms O₂⁻ and other active species. CB electrons also directly react with Cr (VI) and reduced it to Cr (III) as final product due to low stability of Cr(V) and Cr(IV) with accordance to previous

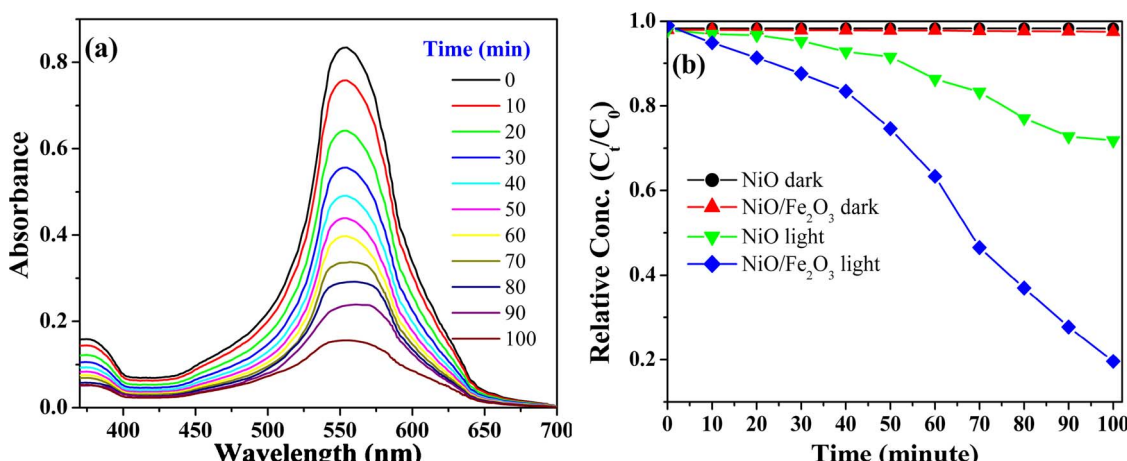


Fig. 10. (a) Spectral change of RhB dye solution in presence of light and NiO/Fe₂O₃ thin films. (b) Reaction profile of RhB degradation against specific time intervals under various conditions.

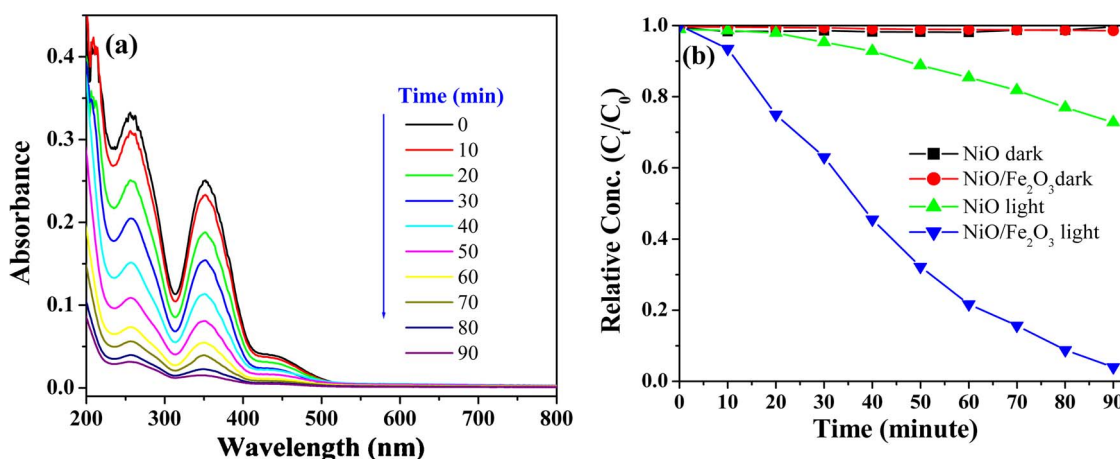
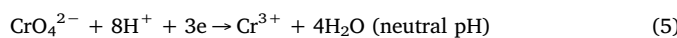
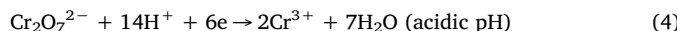


Fig. 11. (a) Photocatalytic reduction of 100 mL of 5×10^{-4} M Cr (VI) in the presence of NiO/Fe₂O₃ thin films. (b) Reaction profile of Cr (VI) reduction against specific time intervals under various conditions.

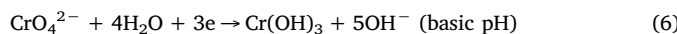
observations by Vinu et al. [65].

3.6.1. Effect of pH and reusability

The effect of pH on the visible light-driven photocatalytic reduction of Cr(VI) in the presence of NiO/Fe₂O₃ thin films was examined by varying initial pH from 1.5 to 7. It was observed that photocatalytic reduction of Cr(VI) decreases with increasing pH (Fig. S13). The reduction in acidic and neutral pH occurred through the following mechanism [66].



In basic pH, Cr³⁺ precipitates as the Cr(OH)₃ onto the catalytic substrate and hence catalytic process becomes less efficient.



The reusability and stability of the photocatalysts is a vital characteristic to judge about efficiency of catalysts and therefore, it is imperative to study the stability of the as-synthesized thin films after photocatalytic reduction of Cr(VI). The results reveal that the photocatalytic activity of NiO/Fe₂O₃ thin films decreases after sixth cycles of photoreduction of Cr(VI). The decrease of reduction ability may be attributed due to the deposition of small amounts of Cr(III) onto the surface of NiO/Fe₂O₃ after each cycle.

4. Conclusions

In summary, a novel binder-free heterostructure based on NiO/Fe₂O₃ thin film has been constructed by a new technique. The synthesized NiO/Fe₂O₃ heterostructure is quite effective to sense glucose. High sensitivity, long linear range, and short detection limit etc. are the salient features of the proposed sensor. Interference study shows that the concentrations of AA, UA and DA have no significant affect towards glucose sensing. The modified electrode was successfully applied to measure glucose concentration in human blood sample. The coupled NiO/Fe₂O₃ heterostructure also shows high catalytic performance towards electro-oxidation methanol in alkaline media. Hence, NiO/Fe₂O₃ heterostructure is versatile and is a promising new material for bio-sensor devices, and can be used as a single platform to oxidise glucose, methanol even at very low concentration. Further, the synthesized NiO/Fe₂O₃ heterostructure shows enhanced photocatalytic activity towards decomposition of phenol, commercial dyes and photo reduction of Cr (VI). The results indicate a great potential use of NiO/Fe₂O₃ as a pollutant cleanup for environmental interest.

Acknowledgements

The author Dr. S. Jana is grateful to DST-SERB Govt. of India for providing him National Post Doctoral Fellowship (Sanction No. SERB/F/3407/2016-17, File No. PDF/2016/000107) for carrying out research at Department of Chemistry, University of Calcutta. Thanks to voluntary individuals Aparna Jana, Sampad Jana for real blood sample analysis. The authors acknowledge Department of Chemistry, University of Calcutta and IEST, Shibpur for instrumental facilities and IIT Kharagpur for some characterizations.

Appendix A. Supplementary data

Supplementary material related to this article can be found, in the online version, at doi:<https://doi.org/10.1016/j.apcatb.2018.03.038>.

References

- [1] M.N. Niu, F. Huang, L.F. Cui, P. Huang, Y.L. Yu, Y.S. Wang, Hydrothermal synthesis, structural characteristics, and enhanced photocatalysis of SnO₂/α-Fe₂O₃ semiconductor heterostructures, *ACS Nano* 4 (2010) 681–688.
- [2] X. Wu, P. Jiang, Y. Ding, W. Cai, S.S. Xie, Z.L. Wang, Mismatch strain induced formation of ZnO/ZnS heterostructured rings, *Adv. Mater.* 19 (2007) 2319–2323.
- [3] S.I. Kim, J.S. Lee, H.J. Ahn, H.K. Song, J.H. Jang, Facile route to an efficient NiO supercapacitor with a three-dimensional nano network morphology, *ACS Appl. Mater. Interfaces* 5 (2013) 1596–1603.
- [4] J.M. Ma, J.Q. Yang, L.F. Jiao, Y.H. Mao, T.H. Wang, X.C. Duan, J.B. Lian, W.J. Zheng, NiO nanomaterials: controlled fabrication, formation mechanism and the application in lithium-ion battery, *CrystEngComm* 14 (2012) 453–459.
- [5] B. Liu, H.Q. Yang, H. Zhao, L.J. An, L.H. Zhang, R.Y. Shi, L. Wang, L. Bao, Y. Chen, Synthesis and enhanced gas-sensing properties of ultralong NiO nanowires assembled with NiO nanocrystals, *Sens. Actuators B* 156 (2011) 251–262.
- [6] Q. Dong, S. Yin, C.S. Guo, X.Y. Wu, N. Kumada, T. Takei, A. Miura, Y. Yonesaki, Y. Sato, Single-crystalline porous NiO nanosheets prepared from β-Ni(OH)₂ nanosheets: magnetic property and photocatalytic activity, *Appl. Catal. B: Environ.* 14 (2014) 7741–7747.
- [7] Y.Z. Zheng, H.Y. Ding, M.L. Zhang, Preparation and electrochemical properties of nickel oxide as a supercapacitor electrode material, *Mater. Res. Bull.* 44 (2009) 403–407.
- [8] F. Le Formal, M. Gratzel, K. Sivula, Controlling photoactivity in ultrathin hematite films for solar water-splitting, *Adv. Funct. Mater.* 20 (2010) 1099–1107.
- [9] A. Kay, I. Cesar, M. Gratzel, New benchmark for water photooxidation by nanostuctured α-Fe₂O₃ films, *J. Am. Chem. Soc.* 128 (2006) 15714–15721.
- [10] D.K. Zhong, J. Sun, H. Inumaru, D.R. Gamelin, Solar water oxidation by composite catalyst/α-Fe₂O₃ photoanodes, *J. Am. Chem. Soc.* 131 (2009) 6086–6087.
- [11] C. Wang, X. Cheng, X. Zhou, P. Sun, X. Hu, K. Shimano, G. Lu, N. Yamazoe, Hierarchical α-Fe₂O₃/NiO composites with a hollow structure for a gas sensor, *ACS Appl. Mater. Interfaces* 6 (2014) 12031–12037.
- [12] Q.-q. Xiong, J.-p. Tu, X.-h. Xia, X.-y. Zhao, C.-d. Gu, X.-l. Wang, A three-dimensional hierarchical Fe₂O₃@NiO core/shell nanorod array on carbon cloth: a new class of anode for high-performance lithium-ion batteries, *Nanoscale* 5 (2013) 7906–7912.
- [13] Y. Chen, R. Cai, Y. Yang, C. Liu, A. Yuan, H. Yang, X. Shen, Cyanometallic frameworks derived hierarchical porous Fe₂O₃/NiO microflowers with excellent lithium-storage property, *J. Alloys Compd.* 698 (2017) 469–475.

[14] G.J. Sun, H. Khele, J.K. Lee, S. Choi, S. Lee, C. Lee, H₂S gas sensing properties of Fe₂O₃ nanoparticle-decorated NiO nanoplate sensors, *Surf. Coat. Technol.* 307 (2016) 1088–1095.

[15] Y.W. Phuan, M.N. Chong, J.D. Ocon, E.S. Chan, A novel ternary nanostructured carbonaceous-metal-semiconductor eRGO/NiO/α-Fe₂O₃ heterojunction photo-anode with enhanced charge transfer properties for photoelectrochemical water splitting, *Solar Energy Mater. Solar Cells* 169 (2017) 236–169244.

[16] R. Rajendran, Z. Yaakob, M.A.M. Teridi, A.S.M. Rahaman, K. Sopian, Preparation of nanostructured p-NiO/n-Fe₂O₃ heterojunction and study of their enhanced photoelectrochemical water splitting performance, *Mater. Lett.* 133 (2014) 123–126.

[17] X. Shen, Q. Liu, Z. Ji, G. Zhu, H. Zhou, K. Chen, Controlled synthesis and gas sensing properties of porous Fe₂O₃/NiO hierarchical nanostructures, *CrystEngComm* 17 (2015) 5522–5529.

[18] G. Das, R.M. Tesfaye, Y. Won, H.H. Yoon, NiO-Fe₂O₃ based graphene aerogel as urea electrooxidation catalyst, *Electrochim. Acta* 237 (2017) 171–176.

[19] Y. Liu, H. Teng, H.Q. Hou, T.Y. You, Nonenzymatic glucose sensor based on renewable electrospun Ni nanoparticle-loaded carbon nanofiber paste electrode, *Biosens. Bioelectron.* 24 (2009) 3329–3334.

[20] A. Salimi, M. Roushani, Non-enzymatic glucose detection free of ascorbic acid interference using nickel powder and nafion sol-gel dispersed renewable carbon ceramic electrode, *Electrochim. Commun.* 7 (2005) 879–887.

[21] M. Shamsipur, M. Najafi, M.R.M. Hosseini, Highly improved electrooxidation of glucose at a nickel(II) oxide/multi-walled carbon nanotube modified glassy carbon electrode, *Bioelectrochemistry* 77 (2010) 120–124.

[22] W. Lv, F.M. Jin, Q. Guo, Q.H. Yang, F. Kang, DNA-dispersed graphene/NiO hybrid materials for highly sensitive non-enzymatic glucose sensor, *Electrochim. Acta* 73 (2012) 129–135.

[23] D.K. William, D.C. James, J.M. Oliver, L.B. Deborah, A.K. Edward, C.K. Krzysztof, R.S. Stuart, C.M. Lukehart, Pt–Ru and Pt–Ru–P/carbon nanocomposites: synthesis, characterization, and unexpected performance as direct methanol fuel cell (DMFC) anode catalysts, *J. Phys. Chem.* 107 (2003) 5467–5474.

[24] K.W. Park, J.H. Choi, B.K. Kwon, S.A. Lee, Y.E. Sung, Chemical and electronic effects of Ni in Pt/Ni and Pt/Ru/Ni alloy nanoparticles in methanol electrooxidation, *J. Phys. Chem. B* 106 (2002) 1869–1877.

[25] H.J. Qiu, X. Shen, J.Q. Wang, A. Hirata, T. Fujita, Y. Wang, M.W. Chen, Aligned nanoporous Pt–Cu bimetallic microwires with high catalytic activity toward methanol electrooxidation, *ACS Catal.* 5 (2015) 3779–3785.

[26] X. Sun, K. Jiang, N. Zhang, S. Guo, X. Huang, Crystalline control of {111} bounded Pt₃Cu nanocrystals: multiply-twinned Pt₃Cu icosahedra with enhanced electrocatalytic properties, *ACS Nano* 9 (2015) 7634–7640.

[27] H. Cao, Z. Fan, G. Hou, Y. Tang, G. Zheng, Ball-flower-shaped Ni nanoparticles on Cu modified TiO₂ nanotube arrays for electrocatalytic oxidation of methanol, *Electrochim. Acta* 125 (2014) 275–281.

[28] H. Zhang, C.D. Gu, M.L. Huang, X.L. Wang, J.P. Tu, Anchoring three-dimensional network structured Ni–P nanowires on reduced graphene oxide and their enhanced electrocatalytic activity towards methanol oxidation, *Electrochim. Commun.* 35 (2013) 108–111.

[29] X. Cui, W. Guo, M. Zhou, Y. Yang, Y. Li, P. Xiao, Y. Zhang, X. Zhang, Promoting effect of Co in Ni_mCo_n (m + n = 4) bimetallic electrocatalysts for methanol oxidation reaction, *ACS Appl. Mater. Interfaces* 7 (2015) 493–503.

[30] A.K. Das, R.K. Layek, N.H. Kim, D. Jung, J.H. Lee, Reduced graphene oxide (RGO)-supported NiCo₂O₄ nanoparticles: an electrocatalyst for methanol oxidation, *Nanoscale* 6 (2014) 10657–10665.

[31] R.H. Tamman, A.M. Fekry, M.M. Saleh, Electrocatalytic oxidation of methanol on ordered binary catalyst of manganese and nickel oxide nanoparticles, *Int. J. Hydrogen Energy* 40 (2015) 275–283.

[32] J.A. Byrne, P.S. Dunlop, J.W. Hamilton, P. Fernandez-Ibanez, I. Polo-Lopez, P.K. Sharma, A.S. Vennard, A review of heterogeneous photocatalysis for water and surface disinfection, *Molecules* 20 (2015) 5574–5615.

[33] X. Hu, H. Ji, F. Chang, Y. Luo, Simultaneous photocatalytic Cr(VI) reduction and 2,4,6-TCP oxidation over g-C₃N₄ under visible light irradiation, *Catal. Today* 224 (2014) 34–40.

[34] H. Abdullah, D.H. Kuo, Photocatalytic performance of Ag and CuBiS₂ nanoparticle-coated SiO₂/TiO₂ composite sphere under visible and ultraviolet light irradiation for azo dye degradation with the assistance of numerous nano p–n diodes, *J. Phys. Chem. C* 119 (2015) 13632–13641.

[35] H. Abdullah, D.H. Kuo, Facile synthesis of n-type (AgIn)_xZn_{2(1-x)}S₂/p-type Ag₂S nanocomposite for visible light photocatalytic reduction to detoxify hexavalent chromium, *ACS Appl. Mater. Interfaces* 7 (2015) 26941–26951.

[36] F. Hashemzadeh, A. Gaffarinejad, R. Rahimi, Porous p-NiO/n-Nb₂O₅ nanocomposites prepared by an EISA route with enhanced photocatalytic activity in simultaneous Cr(VI) reduction and methyl orange decolorization under visible light irradiation, *J. Hazard. Mater.* 286 (2015) 64–74.

[37] X. Pan, Z. Liu, Z. Chen, Y. Cheng, D. Pan, J. Shao, Z. Lin, X. Guan, Investigation of Cr (VI) reduction and Cr(III) immobilization mechanism by planktonic cells and biofilms of *Bacillus subtilis*, *Water. Res.* 55 (2014) 21–29.

[38] H.K. Zhang, H. Lu, J. Wang, J.T. Zhou, M. Sui, Cr(VI) reduction and Cr(III) immobilization by *Acinetobacter* sp. HK-1 with the assistance of a novel quinone/graphene oxide composite, *Environ. Sci. Technol.* 48 (2014) 12876–12885.

[39] M.K. Guria, A.K. Guha, M. Bhattacharya, A green chemical approach for biotransformation of Cr(VI) to Cr(III), utilizing *Fusarium* sp. MMT1 and consequent structural alteration of cell morphology, *J. Environ. Chem. Eng.* 2 (2014) 424–433.

[40] J.R. Memon, S.Q. Memon, M.I. Bhanger, M.Y. Khuhawar, Banana peel: a green and economical sorbent for Cr(III) removal, *Anal. Environ. Chem.* 9 (2008) 20–25.

[41] U. Danis, Chromate removal from water using red mud and crossflow microfiltration, *Desalination* 181 (2005) 135–143.

[42] C. Das, P. Patel, S. De, S.D. Gupta, Treatment of tanning effluent using nanofiltration followed by reverse osmosis, *Sep. Purif. Technol.* 50 (2006) 291–299.

[43] A.A. Atia, Synthesis of a quaternary amine anion exchange resin and study its adsorption behaviour for chromate oxyanions, *J. Hazard. Mater.* 137 (2006) 1049–1055.

[44] S.K. Li, X. Guo, Y. Wang, F.Z. Huang, Y.H. Shen, X.M. Wang, A.J. Xie, Rapid synthesis of flower-like Cu₂O architectures in ionic liquids by the assistance of microwave irradiation with high photochemical activity, *Dalton Trans.* 40 (2011) 6745–6750.

[45] Y.C. Zhang, J. Li, H.Y. Xu, One-step in situ solvothermal synthesis of SnS₂/TiO₂ nanocomposites with high performance in visible light-driven photocatalytic reduction of aqueous Cr(VI), *Appl. Catal. B* 123 (2012) 18–26.

[46] D. Dinda, A. Gupta, S.K. Saha, Removal of toxic Cr(VI) by UV active functionalized graphene oxide for water purification, *J. Mater. Chem. A* 1 (2013) 11221–11228.

[47] S. Jana, P. Mondal, S. Tripathi, A. Mondal, B. Chakraborty, Electrochemical synthesis of FeS₂ thin film: an effective material for peroxide sensing and terephthalic acid degradation, *J. Alloys Compd.* 646 (2015) 893–899.

[48] S. Oswald, W. Brückner, XPS depth profile analysis of non-stoichiometric NiO films, *Surf. Interface Anal.* 36 (2004) 17–22.

[49] Simelys Hernández, Valentina Cauda, Diana Hidalgo, Vivian Farías Rivera, Diego Manfredi, Angelica Chiodoni, Fabrizio C. Pirri, Fast and low-cost synthesis of 1D ZnO–TiO₂ core–shell nanoarrays: characterization and enhanced photoelectrochemical performance for water splitting, *J. Alloys Compd.* 615 (2014) S530–S537.

[50] C.Z. Zhao, C.L. Shao, M.H. Li, K. Jiao, Flow injection analysis of glucose without enzyme based on electrocatalytic oxidation of glucose at a nickel electrode, *Talanta* 71 (2007) 1769–1773.

[51] A. Safavi, N. Maleki, E. Farjami, Fabrication of a glucose sensor based on a novel nanocomposite electrode, *Biosens. Bioelectron.* 24 (2009) 1655–1660.

[52] L.M. Lu, L. Zhang, F.L. Qu, H.X. Lu, X.B. Zhang, Z.S. Wu, S.Y. Huan, Q.A. Wang, G.L. Shen, R.Q. Yu, A nano-Ni based ultrasensitive nonenzymatic electrochemical sensor for glucose: enhancing sensitivity through a nanowire array strategy, *Biosens. Bioelectron.* 25 (2009) 218–223.

[53] J. Chen, J. Zheng, A highly sensitive non-enzymatic glucose sensor based on trentella-like Ni(OH)₂ and Au nanohybrid films, *J. Electroanal. Chem.* 749 (2015) 83–88.

[54] L. Luo, F. Li, L. Zhu, Y. Ding, Z. Zhang, D. Deng, B. Lu, Nonenzymatic glucose sensor based on nickel(II)oxide/ordered mesoporous carbon modified glassy carbon electrode, *Colloids Surf. B: Biointerfaces* 102 (2013) 307–311.

[55] L. Zhang, S. Yuan, X. Lu, Amperometric nonenzymatic glucose sensor based on a glassy carbon electrode modified with a nanocomposite made from nickel (II) hydroxide nanoplates and carbon nanofibers, *Microchim. Acta* 181 (2014) 365–372.

[56] R.A. Soomro, Z.H. Ibupoto, M.I.S. Abro, M. Willander, Electrochemical sensing of glucose based on novel hedgehog-like NiO nanostructures, *Sens. Actuators B* 209 (2015) 966–974.

[57] H. Zhang, S. Liu, Nanoparticles-assembled NiO nanosheets templated by graphene oxide film for highly sensitive non-enzymatic glucose sensing, *Sens. Actuators B* 238 (2017) 788–794.

[58] D. Wang, C. Song, Z. Hu, X. Fu, Fabrication of hollow spheres and thin films of nickel hydroxide and nickel oxide with hierarchical structures, *J. Phys. Chem. B* 109 (2005) 1125–1129.

[59] M.R. Hoffmann, S.T. Martin, W. Choi, D.W. Bahnemann, Environmental applications of semiconductor photocatalysis, *Chem. Rev.* 95 (1995) 69–96.

[60] E.Y. Sun, L. Josephson, K.A. Kelly, R. Weissleder, Development of nanoparticle libraries for biosensing, *Bioconjugate Chem.* 17 (2006) 109–113.

[61] T.C. Cheng, K.S. Yao, N. Yeh, C.I. Chang, H.C. Hsu, F. Gonzalez, C.Y. Chang, Bactericidal effect of blue LED light irradiated TiO₂/Fe₂O₄ particles on fish pathogen in seawater, *Thin Solid Films* 519 (2011) 5002–5006.

[62] T. Zhu, J.S. Chen, X.W. Lou, Highly efficient removal of organic dyes from waste water using hierarchical NiO spheres with high surface area, *J. Phys. Chem. C* 116 (2012) 6873–6878.

[63] D. Li, H. Haneda, Morphologies of zinc oxide particles and their effects on photocatalysis, *Chemosphere* 5 (2003) 129–137.

[64] A. Sobczynski, L. Duzcmal, W. Zmudzinski, Phenol destruction by photocatalysis on TiO₂: an attempt to solve the reaction mechanism, *J. Mol. Catal. A: Chem.* 213 (2004) 225–230.

[65] R. Vinu, G. Madras, Kinetics of simultaneous photocatalytic degradation of phenolic compounds and reduction of metal ions with nano-TiO₂, *Environ. Sci. Technol.* 42 (2008) 913–919.

[66] M.I. Litter, Heterogeneous photocatalysis; transition metal ions in photocatalytic systems, *Appl. Catal. B* 23 (1999) 89–114.